


Paramagnetic phases of two-dimensional magnetic materials

Xiao-Yan Chen, Meng-Qiu Long, and Yun-Peng Wang ^{*}

School of Physics and Electronics, Hunan Key Laboratory for Super-Micro Structure and Ultrafast Process, Central South University, 932 South Lushan Road, Changsha 410083, People's Republic of China

 (Received 26 May 2020; revised 23 September 2020; accepted 2 December 2020; published 15 December 2020)

The magnetic long-range ordering states of van der Waals magnets at low temperatures have gained much interest, yet their high-temperature paramagnetic states remain largely unexplored. In this paper, we apply the disordered local moment picture for describing the paramagnetic states of two-dimensional magnetic semiconductors. We calculate the electronic structure of paramagnetic phases of CrI_3 , CrSiTe_3 , and NiPS_3 using the density functional theory with static Hubbard corrections. The semiconducting electronic structures are successfully reproduced without any inclusion of dynamical correlation effects. The local electronic structure of magnetic ions in the paramagnetic phase resembles those in the magnetically ordered phase. The band structures of the paramagnetic phases are also analyzed. The itinerant ferromagnet Fe_3GeTe_2 is also briefly discussed where the disordered local moment picture is not applicable due to the coexistence of itinerant and local magnetism.

DOI: [10.1103/PhysRevB.102.214417](https://doi.org/10.1103/PhysRevB.102.214417)

I. INTRODUCTION

Low-dimensional magnets with van der Waals (vdW) bonding between layers have gained intensive attention recently [1–3]. The persistence of long-range magnetic order in the few layers even in the monolayers has been demonstrated in several vdW magnets, including $M\text{PS}_3$ (M : transition metals) [4–7], CrI_3 [8], CrXTe_3 ($X = \text{Si, Ge}$) [9], Fe_3GeTe_2 [10,11], etc. Detection of magnetically ordered states in ultrathin films of vdW magnetic materials relies on the spontaneously broken symmetries induced by magnetically long-range ordering. The breaking of time-reversal symmetry leads to magneto-optical Kerr effect in ferromagnetic vdW thin films. Although the cancellation of magnetization in antiferromagnetic vdW magnets prevents the magneto-optical Kerr response, the breaking of rotational symmetry splits the phonon modes those were degenerate in the paramagnetic phase [12]. Angle-resolved photoemission spectroscopy (ARPES) has been employed to unveil the band structure of the paramagnetic phases of CrSiTe_3 (Ref. [13]), CrGeTe_3 (Ref. [14]), Fe_3GeTe_2 (Refs. [15,16]), and CrI_3 and VI_3 (Ref. [17]). A thorough insight of the paramagnetic state, thus, helps us to deepen the understanding of magnetically ordered state, especially the symmetry-breaking role played by magnetic orders.

Theoretical treatment of paramagnetic states is nontrivial. The paramagnetic states were simulated in some studies by using nonmagnetic density functional theory (DFT) calculations, however, the predicted metallic states disagree with experimental data [13,18]. The inclusion of dynamical correlation effects by using the dynamical mean-field theory eventually opens an energy gap, therefore, magnetic vdW semiconductors were classified as Mott insulators [13,19].

On the other hand, the ferromagnetic state was predicted to be semiconducting using ordinary DFT calculations even without inclusion of correlation effects. The local magnetic moment is the key concept to resolve the issue. The intra-atomic exchange coupling leads to formation of local magnetic moment on each transition-metal ion. The presence of local magnetic moments in paramagnetic phases is evidenced by the Curie-Weiss law of the magnetic susceptibility. When the paramagnetic phases are treated as nonmagnetic, the constraint of spin degeneracy forces the d orbitals of transition-metal ions to be partially occupied and results in a metallic ground state [13,18]. Therefore, local spin density will be explicitly taken into account for a correct description of the paramagnetic phase.

The studies of the paramagnetic phases of magnetic materials have been focused on $3d$ -transition metals, their alloys, and compounds [20]. Strong magnets possess local moments on magnetic ions, and their paramagnetic phases are characterized by randomly oriented local moments due to thermal fluctuations. In the disordered local moment (DLM) picture [21–26], it is further assumed that the timescale for local-moment flipping is much longer than that for electron hopping. The electronic structure of one of the random magnetic configurations can be computed within the Born-Oppenheimer approximation with the spin treated as the slow degree of freedom. Macroscopic properties of paramagnetic phase can be obtained by an ensemble average over disordered local-moment configurations using the coherent potential approximation (CPA) [26] or the special quasirandom structures (SQS) [27,28].

In this paper, we investigate the paramagnetic phases well above the Neel/Curie temperatures of prototypical magnetic vdW semiconductors CrI_3 , CrSiTe_3 , and NiPS_3 . We combine the DLM-SQS method and the DFT to calculate their electronic structures. The transition between magnetically ordered phase and the paramagnetic phase is out of the scope of this

^{*}yunpengwang@csu.edu.cn

paper. The semiconducting energy gaps in the paramagnetic (PM) phases are reproduced without the inclusion of any dynamical correlation effect. The local density of states projected on each transition-metal ion in the PM phase remains the same as in the magnetically ordered phase. We also briefly discuss the case of itinerant ferromagnet Fe_3GeTe_2 and identify the existence of itinerant and localized magnetism.

The rest of the paper is organized as follows. The simulation methods were detailed in Sec. II. Calculation results of electronic structure of CrI_3 and CrSiTe_3 are presented in Sec. III A. The electronic structure and optical conductivity of NiPS_3 are discussed in Sec. III B. In Sec. III C, we briefly discuss the mixed itinerant and local magnetism in metallic Fe_3GeTe_2 . Conclusions of this paper are given in Sec. IV.

II. COMPUTATIONAL METHODS

The disordered local magnetic moments in the paramagnetic phases are simulated using the special quasirandom structures method [27]. For CrI_3 and CrSiTe_3 , we build 4×4 and $3 \times 3 \times 1$ supercells for the monolayer and bulk, respectively. Supercells of 3×2 and $3 \times 2 \times 2$ are used for the monolayer and bulk of NiPS_3 . The SQS was generated using the MCSQS program [29] in the ALLOY THEORETIC AUTOMATED TOOLKIT package [30,31] with the cutoff distance of clusters set to 8 Å.

First-principles calculations were carried out using spin-polarized DFT in the projector augmented-wave framework as implemented in the VASP code [32–36]. We use the Perdew-Burke-Ernzerhof [37] parametrization of the generalized gradient approximation (GGA) for the exchange-correlation functional. The semiempirical D2 van der Waals correction of Grimme [38] was added for the bulk systems. The first Brillouin zone was sampled by uniform Monkhorst-Pack meshes of 5×5 and $5 \times 5 \times 3$ for monolayers and bulks, respectively. The energy cutoff of the plane waves is set to 400 eV. We took the experimental values for the lattice constants of all the materials. The atomic positions in the primitive cells were fully optimized with the magnetic structures set to their ground states, until the residual forces on all atoms are less than 0.01 eV/Å. The supercells were constructed by repeating primitive cells but without further structural relaxations.

The band structures of the paramagnetic phases were unfolded to the first Brillouin zone of the corresponding primitive cell using the effective band-structure approach [39,40] as implemented in the BANDUP code [41,42]. The frequency-dependent dielectric function was calculated within the independent-particle approximation. The spin-orbit coupling effect is ignored in our DFT calculations. The magnetocrystalline anisotropy resulting from the spin-orbit coupling is crucial for the magnetic ground states and the magnetic phase transitions. The spin-orbit coupling effect is less important than the magnetic exchange effect for comparing electronic structures of magnetically ordered and disordered phases.

III. RESULTS

We first analyze the energy splitting of d orbitals of Cr^{3+} and Ni^{2+} ions in CrI_3 , CrSiTe_3 , and NiPS_3 compounds. These d orbitals split by the octahedral crystal field to t_{2g} and e_g ,

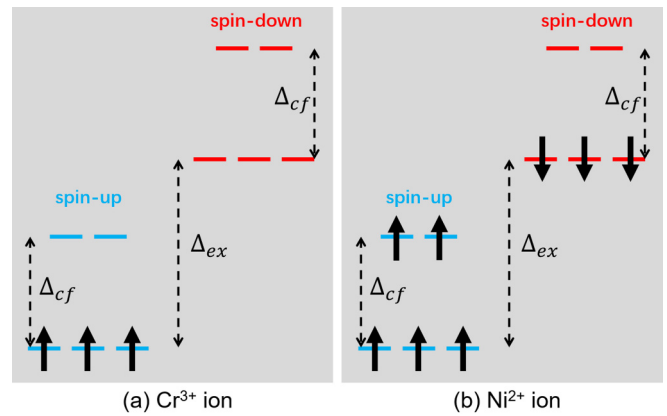


FIG. 1. The energy levels of the d shell of (a) Cr^{3+} (d^3) and (b) Ni^{2+} (d^8) ions. The t_{2g} and e_g orbitals of the same spin channel are splitted by crystal field effect ($\Delta_{cf} \sim 1.5$ eV). The spin-up and spin-down channels are splitted due to intra-atomic exchange interactions ($\Delta_{ex} \sim 3$ eV).

and the crystal-field splitting energy is $\Delta_{cf} \sim 1.5$ eV. The intra-atomic exchange interaction induces spin splitting of $\Delta_{ex} \sim 3$ eV. In real materials, the values of Δ_{cf} and Δ_{ex} are corrected by orbital hybridization with ligands and the intra-atomic Coulomb repulsive interaction. The energy levels of Cr^{3+} (d^3) and Ni^{2+} (d^8) ions within the mean-field picture are schematically shown in Fig. 1. The lowest-lying t_{2g} orbitals in the spin-up channel are fully occupied in the Cr^{3+} ion. Electrons occupy upon the spin-down t_{2g} orbitals in the Ni^{2+} ion. As a result, the occupation numbers on d orbitals are integers. Neglecting the hybridization with ligands, the energy gaps of Cr^{3+} - and Ni^{2+} -containing compounds are estimated to be the crystal-field splitting energy $\Delta_{cf} \sim 1.5$ eV. Indeed, the experimental band gaps of CrI_3 , CrSiTe_3 , and NiPS_3 are on the order of 1 eV. Note that the energies and occupations of d -shell energy levels are determined by the transition-metal ions themselves and are, thus, independent on the global magnetic moment configuration. Therefore, one expects that the local electronic structure of the transition-metal ion in paramagnetic states remains the same as in the magnetically ordered state. The paramagnetic state is expected to possess a similar energy gap with magnetically ordered states.

A. CrI_3 and CrSiTe_3

In this section, we discuss CrI_3 and CrSiTe_3 due to the close similarity. Both CrI_3 and CrSiTe_3 exhibit ferromagnetic ordering at low temperatures with the Curie temperatures of 61 and 33 K, respectively. Both compounds are semiconductors exhibiting electronic energy gaps below and above their Curie temperatures. The energy gap of CrI_3 is 1.1–1.2 eV according to photoluminescence [43,44] and photocurrent [44] experiments and is independent of the temperature [43]. CrSiTe_3 is an indirect band-gap semiconductor with an experimental indirect band gap of 0.4 eV and a direct band gap of 1.2 eV [45]. Our DFT-GGA calculation of the ferromagnetic (FM) states predict energy gaps of 0.8 eV for CrI_3 and 0.4 eV for CrSiTe_3 .

The DOS of bulk and monolayer CrI_3 in the FM and PM phases are shown in Fig. 2. Results for CrSiTe_3 are shown in

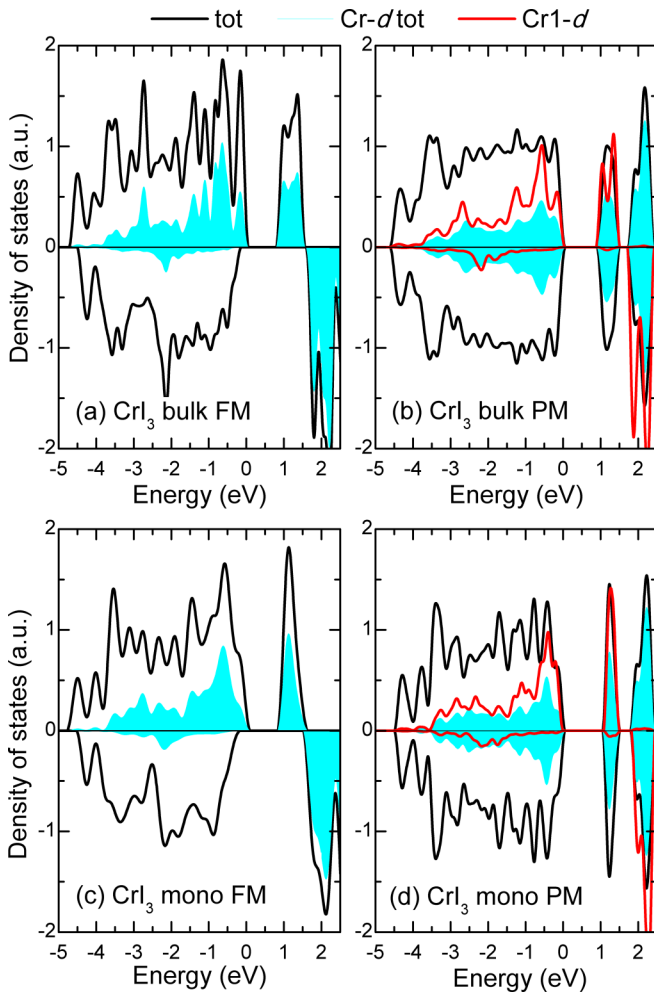


FIG. 2. Calculated density of states (DOS) of (a) and (b) CrI_3 bulk and (c) and (d) monolayer in the (a) and (c) FM and (b) and (d) PM states.

Fig. 3. The projected DOS on Cr- d orbitals (hereafter denoted as PDOS-Cr) are also plotted. For the FM states as shown in Figs. 2(a) and 2(c) and Figs. 3(a) and 3(c), the PDOS-Cr in the spin-up channel is characterized by a broad peak between -4 and 0 eV corresponding to the occupied t_{2g} orbitals, and a sharp peak at 1 eV corresponding to the e_g orbitals. The PDOS on t_{2g} orbitals are strongly broadened due to the hybridization with ligands. In the spin-down channel, the peak in the total DOS around 3 eV is dominated by the unoccupied t_{2g} orbitals. The calculated DOS agrees qualitatively with the energy-level diagram in Fig. 1. Comparing with the monolayer, the spin-up DOS peak at 1 eV of bulk are slightly wider due to interlayer hybridizations.

The calculated DOS of the paramagnetic state are shown in Figs. 2(b) and 2(d) for CrI_3 and Figs. 3(b) and 3(d) for CrSiTe_3 . The PM states of CrI_3 and CrSiTe_3 possess semiconducting electronic structures. As for the value of the energy gap, if one estimates the energy gap as the width of the zero-DOS region, the PM phases have ~ 0.1 -eV larger energy gaps than the corresponding FM phases. If one instead measures the energy gap using the peaks in the DOS, the PM and FM phases show the same energy gaps, in accordance with experimental data [43]. The projected DOS on one of the Cr

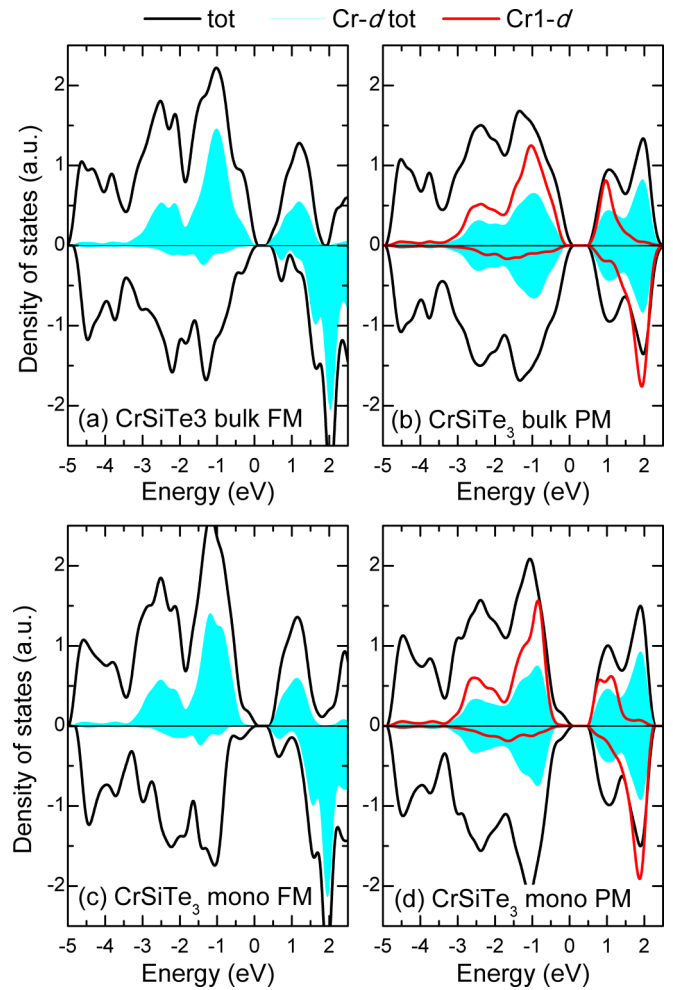


FIG. 3. Calculated DOS of (a) and (b) CrSiTe_3 bulk and (c) and (d) monolayer in the (a) and (c) FM and (b) and (d) PM states.

ions with up local moment (hereafter denoted as PDOS-Cr1) is properly scaled and plotted in Figs. 2(b) and 2(d) and Figs. 3(b) and 3(d) as red lines. The shape of the PDOS-Cr1 in the PM phase is similar to the projected DOS on Cr in the FM phase, indicating that Cr ions in the PM states remain strongly spin polarized. The average value of the local magnetic moments in the PM phase is lower by $0.05\mu_B$ per Cr ion than the FM phase. The calculated local magnetic moments and projected DOS prove that the local electronic structure of each Cr ion is independent of the global magnetic configuration. Our calculation results validate the disordered local moment picture for describing the paramagnetic phase of CrI_3 and CrSiTe_3 . Both the calculated local magnetic moments and the band gaps agree well with experimental data. Note that our calculations were performed using the ordinary GGA without including static or dynamic correlation effects.

Next, we discuss the band structures of CrI_3 and CrSiTe_3 monolayers in the PM phase. As seen from the DOS, the interlayer interaction plays a minor role on the electronic structure. Because sizable supercells were employed in the simulations of the paramagnetic phases, the calculated band structures are severely folded. We, therefore, unfolded the band structures to the first Brillouin zone of the primitive cells using the effective band-structure approach [39,40]. The unfolded band structure

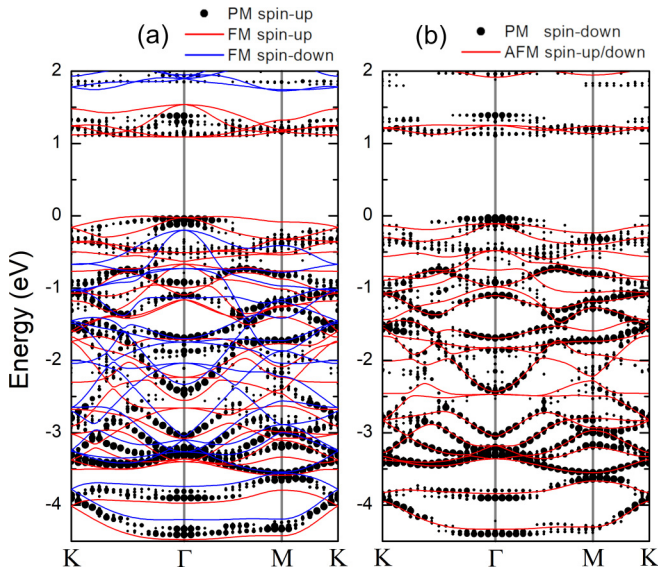


FIG. 4. Band structures of the CrI_3 monolayer in para-, ferro-, and antiferromagnetic phases. Spectral weights of the spin-up and spin-down channels of the paramagnetic phase are shown as black dots in (a) and (b), respectively; the sizes of the black dots represent spectral weights. The band structure of the ferromagnetic phase is shown as lines in (a): red lines for the spin-up channel, and blue lines for the spin-down channel. The band structure of the antiferromagnetic phase is shown as lines in (b): The two spin channels are degenerate.

is characterized by spectral weights at the given energy and k point. The unfolded band structure of the PM phases are shown in Fig. 4 for the CrI_3 monolayer and in Fig. 5 for the CrSiTe_3 monolayer. The spectral weights are represented by the sizes of the black dots in these figures.

Figure 4 shows the band structure of the CrI_3 monolayer in the PM, FM, and the AFM phases. The PM band structure in

the spin-up channel is shown as the black dots in Fig. 4(a); the spin-down channel is shown in Fig. 4(b). There is a negligible difference between the spin-up and the spin-down channels.

The band structure of the FM phase is also plotted in Fig. 4(a): Red lines represent the spin-up channel, and blue lines represent the spin-down channel. If one looks at the PM bands with significant spectral weights, one can find counterparts in the FM band structure exhibiting a similar energy dispersion relation. Yet the strong spin splitting of the FM bands prevents one from setting up a one-to-one correspondence with the PM bands.

Figure 4(b) shows the band structure of the AFM phase. One immediately notes a much better agreement between the PM bands and the AFM bands especially below -1 eV. There are yet minor disagreements between the PM and the AFM bands, for instance, the conduction bands and the valence bands near the band gap. Despite these minor disagreements, the ordered AFM phase is a fairly good representation of the disordered PM phase in the perspective of the band structure.

The case of the monolayer CrSiTe_3 is shown in Fig. 5, including the band structures of the PM, FM, and AFM phases. The calculated PM band structure agrees well with ARPES data reported in Ref. [13]: There are two clear bands within 1 eV below the energy gap. Comparing the PM band structure with those of the FM and AFM phases, one can draw the same conclusion as for the CrI_3 case: The agreement of the PM bands with the AFM bands is much better than with the FM bands. The AFM bands coincide with the PM bands near the valence-band edge and for the low-lying bands below -3 eV. Within the energy range between -0.5 and -2.5 eV, the PM bands smear out, that is, the spectral weights within this energy range are significantly reduced with respect to the bands below -3 eV. The intermixing of two spin channels in the disordered PM phase will be the reason for the spectral weight smearing.

B. NiPS_3

The NiPS_3 compound possesses an AFM order below 154 K. In the AFM state, the local magnetic moments of Ni cations align parallel along one in-plane zigzag direction, whereas the neighboring zigzag chains are coupled antiferromagnetically. X-ray absorption and photoemission data suggested NiPS_3 as a self-doped insulator with negative charge transfer. The valence-band edge is dominated by S ligand anions whereas the conduction-band edge is dominated by Ni [46]. Our GGA calculation of the AFM state predicts a semiconducting ground state with an energy gap of 0.6 eV, which is smaller than the experimental energy gap of 1.8 eV [46]. According to the energy-level diagram shown in Fig. 1, we attribute this energy gap as dominated by the crystal-field splitting (Δ_{cf}) of the spin-down channel. A more severe issue of the GGA calculation is that, the valence-band edge is predicted to be dominated by Ni, contradicting with the negative charge transfer nature of NiPS_3 . We, therefore, included a static Hubbard correction of $U_{\text{eff}} = 4$ eV in order to reproduce the band gap and the negative charge-transfer nature. Comparing with the DOS calculated by GGA (not shown here), addition of Hubbard $U_{\text{eff}} = 4$ eV pushes the occupied Ni- d orbitals down in energy by ~ 2 eV, which weakens the

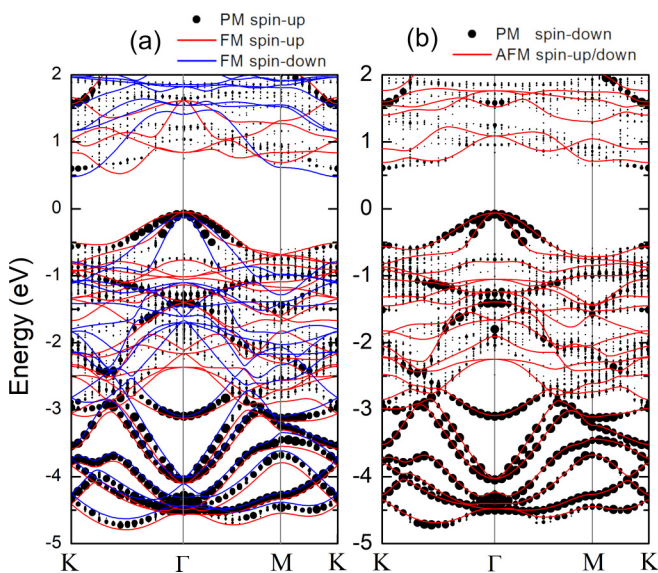


FIG. 5. Band structures of the CrSiTe_3 monolayer in para-, ferro-, and antiferromagnetic phases. The notations are the same as in Fig. 4.

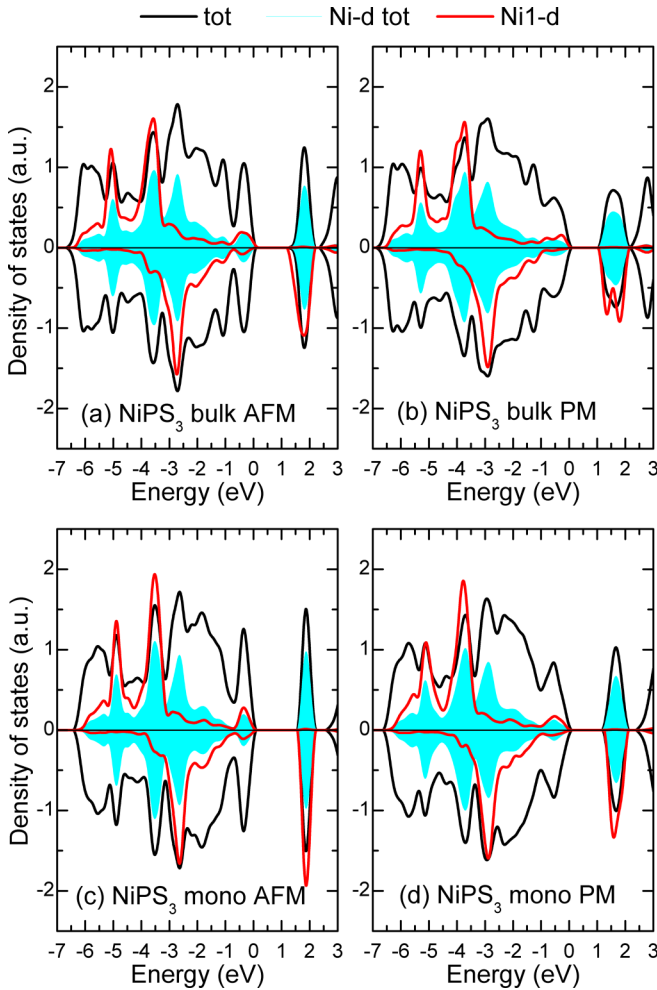


FIG. 6. (a) and (b) Calculated DOS of NiPS_3 bulk and (c) and (d) monolayer in the (a) and (c) AFM and (b) and (d) PM states.

contribution of Ni to the valence-band edge. Figure 6(a) shows the calculated DOS of bulk NiPS_3 in the AFM state using the GGA + U method. The valence-band edge is contributed mainly by S, although the Ni-S hybridization brings a small Ni weight. The monolayer NiPS_3 possesses a very similar DOS, see Fig. 6(c), except that the peaks in DOS are narrower due to absence of interlayer couplings.

The DOS of the PM states are shown in Figs. 6(b) and 6(d) for bulk and monolayer NiPS_3 . For the AFM state, both the valence- and conduction-band edges contribute narrow peaks to the DOS. In the PM states, both of these DOS peaks broaden significantly due to the disordered magnetic configuration. The DOS projected on one of Ni ions (PDOS-Ni1) with the spin-up local magnetic moment is properly scaled and shown as red lines in Fig. 6. One can attribute the peaks in PDOS-Ni1 to atomic orbitals according to Fig. 1: the t_{2g} orbital at -5 eV and the e_g orbital at -3.5 eV in the spin-up channel, whereas the spin-down t_{2g} orbital is at -3 eV and the e_g orbital is at 2 eV. Comparison of the PDOS-Ni1 (red lines) in Figs. 6(a)–6(d) suggest that the local electronic structures of the Ni ion are almost independent of the magnetic orders. This fact validates the local moment picture for the magnetism in NiPS_3 .

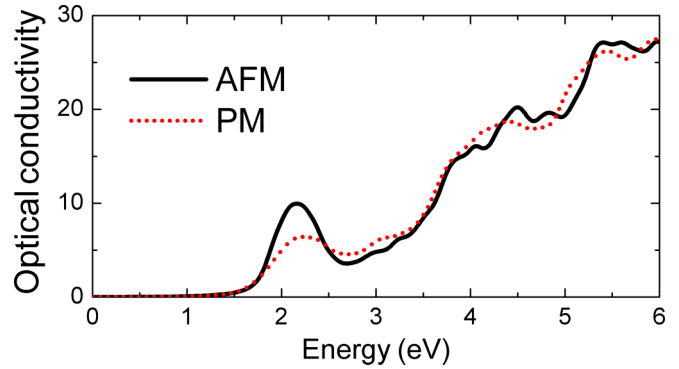


FIG. 7. Calculated optical conductivity of monolayer NiPS_3 in the AFM (the black solid line) and PM (the red dotted line) states.

The disordered local magnetic moments in the PM phase modify the optical property. According to the cluster model analysis in Ref. [46], the ~ 2 -eV electronic transition by photon absorption is allowed only when nearest-neighboring NiS_6 clusters are antiferromagnetically coupled. We calculated the dielectric function $\epsilon(\omega)$ of AFM and PM NiPS_3 . The optical conductivity is related to the dielectric function by $\sigma_1(\omega) = \Im\epsilon(\omega)\omega/4\pi$. The calculated $\sigma_1(\omega)$ as shown in Fig. 7 is characterized by a peak at 2 eV corresponding to the electronic transition across the band gap. In the PM state, the height of the 2-eV peak is substantially reduced compared to the AFM state, in accord with the cluster model analysis of Ref. [46].

The band structures of the NiPS_3 monolayer in the PM, FM, and AFM phases are shown in Fig. 8. The magnetic

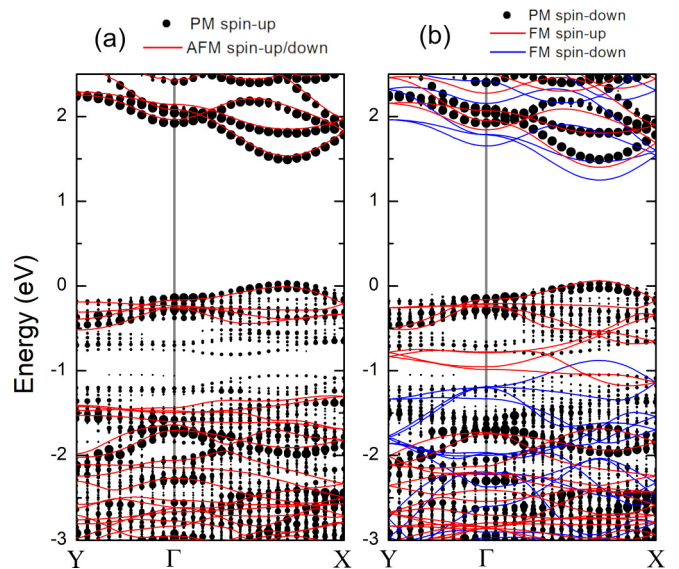


FIG. 8. Band structures of the NiPS_3 monolayer in para-, ferro-, and antiferromagnetic phases. Spectral weights of the spin-up and spin-down channels of the paramagnetic phase are shown as black dots in (a) and (b), respectively; the sizes of the black dots represent spectral weights. The band structure of the antiferromagnetic phase is shown as lines in (a): The two spin channels are degenerate. The band structure of the ferromagnetic phase is shown as lines in (b): red lines for the spin-up channel, and blue lines for the spin-down channel.

ground state of NiPS_3 is AFM, so we first compare the PM band structure with the AFM band structure. The conduction bands and the valence bands near the band gap in the PM phase coincide with those in the AFM phase. There is also fairly good agreement for the bands below -1.5 eV. Noticeable disagreement between the AFM bands and the PM bands occurs between -0.5 and -1.5 eV: The PM bands in this energy range can find no counterparts in the AFM bands; in fact, there are no AFM bands within this energy range. One can find signatures of this disagreement in the DOS. The DOS of the AFM phase [Fig. 6(c)] shows a significant reduction near -1 eV, whereas the DOS of the PM phase [Fig. 6(d)] is much larger. Contrary to the above-discussed CrI_3 and CrSiTe_3 , the AFM phase is no longer a good representation of the disordered PM phase for the case of NiPS_3 . We also plot the band structure of the FM phase in Fig. 8(b). Although the severe disagreement in the conduction band, the FM phase possesses some bands within the $[-0.5, -1.5]$ eV interval. Therefore, it is the locally FM portion in the PM phase that contributes to the electronic states within this energy range.

C. Fe_3GeTe_2

The above two sections are focused on semiconducting vdW magnets. In this section we discuss the case of metallic Fe_3GeTe_2 . Although it is believed that the ferromagnetism of Fe_3GeTe_2 is of the itinerant type [47], some authors instead took the local moment picture [10,16]. A compelling consensus regarding the nature of magnetism in Fe_3GeTe_2 is not yet established. We first assume that the local moment picture is valid for Fe_3GeTe_2 and calculate its electronic structure in the PM state using the DFT-SQS method. There are two nonequivalent Fe sites in the primitive cell, denoted as Fe1 and Fe2 in Fig. 9. Our GGA calculation of the FM state predicts that each Fe1 site possesses a magnetic moment of $2.5\mu_B$, but the local moment on the Fe2 site is only $1.5\mu_B$.

We built a 4×4 supercell of monolayer Fe_3GeTe_2 for DFT-SQS calculations of the PM state. The calculated local moments on Fe1 sites in the PM state scatter between 2.0 and $2.4\mu_B$. The reduction of Fe1 local moments with respect to the FM state (0.1 – $0.5\mu_B$ or 4% – 20%) is sizable yet not severe. As a reference, calculations using the Korringa-Kohn-Rostoker version of the coherent potential approximation (CPA) predicted that the local moment of bcc iron in the PM state is reduced by 15% than the FM state [48].

The calculated local moments on Fe2 sites in the PM state scatter widely between $0.0\mu_B$ and $1.3\mu_B$. In fact, we find that the magnitude of the local moment of a Fe2 site depends on the magnetic configuration of neighboring Fe1 sites. The collapse of local magnetic moments of Fe2 sites completely invalidates the local moment picture for Fe_3GeTe_2 . The magnetism of the Fe2 site is itinerant instead of localized. The magnetism of Fe_3GeTe_2 will be described as local moments on Fe1 sites embedded in the itinerant medium formed by other sites.

Electrons around a site are spin polarized when the formation of a local magnetic moment is accompanied by significant energy reduction. We calculate the total energy reduction due to development of local magnetization as an estimation of the “strongness” of local magnetic moments. As a reference, we

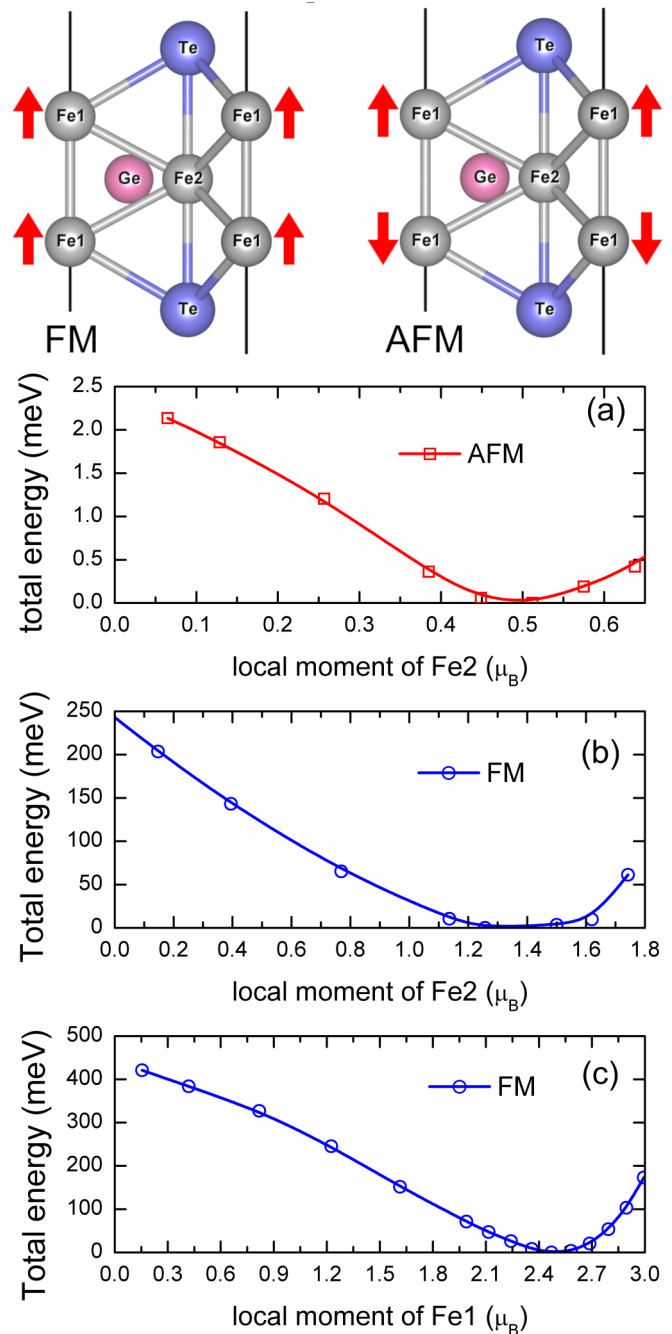


FIG. 9. Total energy of Fe_3GeTe_2 as a function of constrained local magnetic moments. The local moment on the Fe2 site is constrained with local moments on the Fe1 sites in the (a) AFM and (b) FM configurations. (c) The local moment on the Fe1 sites are constrained. The FM and AFM configurations of the Fe1 sites are depicted above (a).

calculated the bcc iron and found that total energy of the FM state is about 500 meV per Fe lower than the nonmagnetic state. The SQS model of the PM state is rather complicated, and we, thus, considered the primitive cell of Fe_3GeTe_2 in two different magnetic configurations where local moments on the Fe1 sites are aligned parallel or antiparallel as shown in Fig. 9. The constrained density functional theory (CDFT) is used for control the directions and magnitudes of local moments.

Figure 9(a) corresponds to the AFM case where the local moments on the Fe1 sites aligned antiparallel to each other. When the local moment on the Fe2 site increases to $0.5\mu_B$, the total energy reaches its minimum. Although the Fe2 site indeed develops a local moment, the accompanied total energy reduction is extremely small (2 meV). Therefore, the local moment on the Fe2 site in the AFM case is quite weak. When the local moments on the Fe1 sites are parallel to each other (the FM case), a local moment of $1.4\mu_B$ develops on the Fe2 site with a total energy reduction of 250 meV as shown Fig. 9(b). In this case the formation of local moment on the Fe2 site is much more energetically favorable than the AFM case. The above two results indicate that the formation of a local moment is not the original nature of the Fe2 site. The local moment on the Fe2 site is not formed by itself but rather induced by the neighboring Fe1 sites. We performed similar CDFT calculations with the local moment on the Fe1 sites constrained. The result is shown in Fig. 9(c). The total energy is reduced by 400 meV per Fe1 site when a $2.5\mu_B$ local moment is formed. The local moments on the Fe1 sites are as strong as in bcc iron from the energetic point of view. Our CDFT calculations prove that Fe1 sites host strong local magnetic moments, whereas electrons at Fe2 sites are itinerant.

IV. CONCLUSIONS

In this paper we have studied the paramagnetism in semiconducting and metallic van der Waals magnets.

We found that the disordered local moment theory works well for semiconducting CrI_3 , CrSiTe_3 , and NiPS_3 . The dynamic correlation effects are not required for describing their paramagnetic phases. This conclusion can be extended to other semiconducting van der Waals magnets, including CrBr_3 , CrCl_3 , CrGeTe_3 , MnPS_3 , FePS_3 , and others. On the other hand, the local moment picture is not applicable for metallic Fe_3GeTe_2 in which case the magnitude of the local moment on Fe2 sites severely depends on the magnetic configuration of neighboring Fe1 sites. Fe_3GeTe_2 possesses a mixed local-itinerant magnetism.

Our conclusions shed light on the understanding and simulating the magnetic dynamics in these materials. The local moment picture holds for semiconducting vdW magnets. Therefore, the extended Heisenberg model and the atomistic Landau-Lifshitz-Gilbert equation are the optimal choice for the simulation of magnetic dynamics [49]. Because of the mixed local-itinerant magnetism of Fe_3GeTe_2 , the Heisenberg model is not applicable, in principle. More sophisticated approaches, such as the many-body perturbation theory in Ref. [50] and references therein, are required for an accurate description of spin excitation in Fe_3GeTe_2 .

ACKNOWLEDGMENTS

This work was supported by the National Natural Science Foundation of China (Grants No. 12004439 and No. 21673296).

-
- [1] K. S. Burch, D. Mandrus, and J.-G. Park, *Nature (London)* **563**, 47 (2017).
 - [2] M. Gibertini, M. Koperski, A. F. Morpurgo, and K. S. Novoselov, *Nat. Nanotechnol.* **14**, 408 (2019).
 - [3] C. Gong and X. Zhang, *Science* **363**, eaav4450 (2019).
 - [4] C.-T. Kuo, M. Neumann, K. Balamurugan, H. J. Park, S. Kang, H. W. Shiu, J. H. Kang, B. H. Hong, M. Han, T. W. Noh *et al.*, *Sci. Rep.* **6**, 20904 (2016).
 - [5] K.-Z. Du, X.-Z. Wang, Y. Liu, P. Hu, M. I. B. Utama, C. K. Gan, Q. Xiong, and C. Kloc, *ACS Nano* **10**, 1738 (2016).
 - [6] J.-U. Lee, S. Lee, J. H. Ryoo, S. Kang, T. Y. Kim, P. Kim, C.-H. Park, J.-G. Park, and H. Cheong, *Nano Lett.* **16**, 7433 (2016).
 - [7] X. Wang, K. Du, Y. Y. F. Liu, P. Hu, J. Zhang, Q. Zhang, M. H. S. Owen, X. Lu, C. K. Gan *et al.*, *2D Mater.* **3**, 031009 (2016).
 - [8] B. Huang, G. Clark, E. Navarro-Moratalla, D. R. Klein, R. Cheng, K. L. Seyler, D. Zhong, E. Schmidgall, M. A. McGuire, D. H. Cobden *et al.*, *Nature (London)* **546**, 270 (2017).
 - [9] C. Gong, L. Li, Z. Li, H. Ji, A. Stern, Y. Xia, T. Cao, W. Bao, C. Wang, Y. Wang *et al.*, *Nature (London)* **546**, 265 (2017).
 - [10] Y. Deng, Y. Yu, Y. Song, J. Zhang, N. Z. Wang, Z. Sun, Y. Yi, Y. Z. Wu, S. Wu, J. Zhu *et al.*, *Nature (London)* **563**, 94 (2018).
 - [11] Z. Fei, B. Huang, P. Malinowski, W. Wang, T. Song, J. Sanchez, W. Yao, D. Xiao, X. Zhu, A. F. May *et al.*, *Nature Mater.* **17**, 778 (2018).
 - [12] K. Kim, J.-U. Lee, and H. Cheong, *Nanotechnology* **30**, 452001 (2019).
 - [13] J. Zhang, X. Cai, W. Xia, A. Liang, J. Huang, C. Wang, L. Yang, H. Yuan, Y. Chen, S. Zhang *et al.*, *Phys. Rev. Lett.* **123**, 047203 (2019).
 - [14] M. Suzuki, B. Gao, K. Koshiishi, S. Nakata, K. Hagiwara, C. Lin, Y. X. Wan, H. Kumigashira, K. Ono, S. Kang *et al.*, *Phys. Rev. B* **99**, 161401(R) (2019).
 - [15] Y. Zhang, H. Lu, X. Zhu, S. Tan, W. Feng, Q. Liu, W. Zhang, Q. Chen, Y. Liu, X. Luo *et al.*, *Sci. Adv.* **4**, eaao6791 (2018).
 - [16] X. Xu, Y. W. Li, S. R. Duan, S. L. Zhang, Y. J. Chen, L. Kang, A. J. Liang, C. Chen, W. Xia, Y. Xu *et al.*, *Phys. Rev. B* **101**, 201104(R) (2020).
 - [17] A. K. Kundu, Y. Liu, C. Petrovic, and T. Valla, *Sci. Rep.* **10**, 15602 (2020).
 - [18] D. T. Larson and E. Kaxiras, *Phys. Rev. B* **98**, 085406 (2018).
 - [19] H.-S. Kim, K. Haule, and D. Vanderbilt, *Phys. Rev. Lett.* **123**, 236401 (2019).
 - [20] I. Abrikosov, A. Ponomareva, P. Steneteg, S. A. Barannikova, and B. Alling, *Curr. Opin. Solid State Mater. Sci.* **20**, 85 (2016).
 - [21] J. Hubbard, *Phys. Rev. B* **19**, 2626 (1979).
 - [22] J. Hubbard, *Phys. Rev. B* **20**, 4584 (1979).
 - [23] J. Hubbard, *Phys. Rev. B* **23**, 5974 (1981).
 - [24] H. Hasegawa, *J. Phys. Soc. Jpn.* **46**, 1504 (1979).
 - [25] H. Hasegawa, *J. Phys. Soc. Jpn.* **49**, 178 (1980).
 - [26] B. L. Gyorffy, A. J. Pindor, J. Staunton, G. M. Stocks, and H. Winter, *J. Phys. F: Met. Phys.* **15**, 1337 (1985).
 - [27] A. Zunger, S.-H. Wei, L. G. Ferreira, and J. E. Bernard, *Phys. Rev. Lett.* **65**, 353 (1990).

- [28] B. Alling, T. Marten, and I. A. Abrikosov, *Phys. Rev. B* **82**, 184430 (2010).
- [29] A. van de Walle, P. Tiwary, M. Jong, D. L. Olmsted, M. Asta, A. Dick, D. Shin, Y. Wang, L.-Q. Chen, and Z.-K. Liu, *Calphad* **42**, 13 (2013).
- [30] A. van de Walle, M. Asta, and G. Ceder, *Calphad* **26**, 539 (2002).
- [31] A. de Walle, *Calphad* **33**, 266 (2009).
- [32] G. Kresse and J. Hafner, *Phys. Rev. B* **47**, 558 (1993).
- [33] G. Kresse and J. Hafner, *Phys. Rev. B* **49**, 14251 (1994).
- [34] G. Kresse and J. Furthmüller, *Comput. Mater. Sci.* **6**, 15 (1996).
- [35] G. Kresse and J. Furthmüller, *Phys. Rev. B* **54**, 11169 (1996).
- [36] G. Kresse and D. Joubert, *Phys. Rev. B* **59**, 1758 (1999).
- [37] J. P. Perdew, K. Burke, and M. Ernzerhof, *Phys. Rev. Lett.* **77**, 3865 (1996).
- [38] S. Grimme, *J. Comput. Chem.* **27**, 1787 (2006).
- [39] V. Popescu and A. Zunger, *Phys. Rev. B* **85**, 085201 (2012).
- [40] Y.-P. Wang and H.-P. Cheng, *Phys. Rev. B* **87**, 245430 (2013).
- [41] P. V. C. Medeiros, S. Stafström, and J. Björk, *Phys. Rev. B* **89**, 041407(R) (2014).
- [42] P. V. C. Medeiros, S. S. Tsirkin, S. Stafström, and J. Björk, *Phys. Rev. B* **91**, 041116(R) (2015).
- [43] K. L. Seyler, D. Zhong, D. R. Klein, S. Gao, X. Zhang, B. Huang, E. Navarro-Moratalla, L. Yang, D. H. Cobden, M. A. McGuire *et al.*, *Nat. Phys.* **14**, 277 (2018).
- [44] Z. Wang, I. Gutiérrez-Lezama, N. Ubrig, M. Kroner, M. Gibertini, T. Taniguchi, K. Watanabe, A. Imamoglu, E. Giannini, and A. F. Morpurgo, *Nat. Commun.* **9**, 2516 (2018).
- [45] L. D. Casto, A. J. Clune, M. O. Yokosuk, J. L. Musfeldt, T. J. Williams, H. L. Zhuang, M.-W. Lin, K. Xiao, R. G. Hennig, B. C. Sales *et al.*, *APL Mater.* **3**, 041515 (2015).
- [46] S. Y. Kim, T. Y. Kim, L. J. Sandilands, S. Sinn, M.-C. Lee, J. Son, S. Lee, K.-Y. Choi, W. Kim, B.-G. Park *et al.*, *Phys. Rev. Lett.* **120**, 136402 (2018).
- [47] B. Chen, J. Yang, H. Wang, M. Imai, H. Ohta, C. Michioka, K. Yoshimura, and M. Fang, *J. Phys. Soc. Jpn.* **82**, 124711 (2013).
- [48] A. J. Pindor, J. Staunton, G. M. Stocks, and H. Winter, *J. Phys. F: Met. Phys.* **13**, 979 (1983).
- [49] O. Eriksson, A. Bergman, L. Bergqvist, and J. Hellsvik, *Atomistic Spin-Dynamics* (Oxford University Press, Oxford, 2017).
- [50] C. Friedrich, E. Şaşıoğlu, M. Müller, A. Schindlmayr, and S. Blügel, *Spin Excitations in Solids from Many-Body Perturbation Theory* (Springer, Berlin, Heidelberg, 2014), pp. 259–301.